The Astrophysical Journal, 635:832–844, 2005 December 20

EVIDENCE FOR A MASSIVE POSTSTARBURST GALAXY AT $z \sim 6.5$

B. Mobasher,[1,2] M. Dickinson,[3] H. C. Ferguson,[1] M. Giavalisco,[1] T. Wiklind,[1,2] D. Stark,[4] R. S. Ellis,[4] S. M. Fall,[1] N. A. Grogin,[5] L. A. Moustakas,[1] N. Panagia,[1,2] M. Sosey,[1] M. Stiavelli,[1] E. Bergeron,[1] S. Casertano,[1] P. Ingraham[6], A. Koekemoer,[1] I. Labbé[7] M. Livio,[1] B. Rodgers,[6] C. Scarlata,[8] J. Vernet,[9] A. Renzini,[9,10] P. Rosati,[9] H. Küntschner,[11] M. Kümmel,[11] J. R. Walsh,[11] R. Chary,[12] P. Eisenhardt,[13] N. Pirzkal,[1] and D. Stern[13]

Received 2005 May 18; accepted 2005 August 29

ABSTRACT

We describe results from a search for high-redshift *J*-band "dropout" galaxies in the portion of the Great Observatories Origins Deep Survey (GOODS) southern field that is covered by extremely deep imaging from the Hubble Ultradeep Field (HUDF). Using observations at optical, near-infrared, and mid-infrared wavelengths from the *Hubble* and *Spitzer Space Telescopes* and the European Southern Observatory Very Large Telescope, we find one particularly remarkable candidate, which we designate HUDF-JD2. Its spectral energy distribution has distinctive features that are consistent with those of a galaxy at $z \sim 6.5$, observed several hundred million years after a powerful burst of star formation that produced a stellar mass of $6 \times 10^{11}\ M_{\odot}$ (for a Salpeter IMF). We interpret a prominent photometric break between the near-infrared and *Spitzer* bandpasses as the 3646 Å Balmer discontinuity. The best-fitting models have low reddening and ages of several hundred Myr, placing the formation of the bulk of the stars at $z > 9$. Alternative models of dusty galaxies at $z \approx 2.5$ are possible, but provide significantly poorer fits to the photometric data. The object is detected with *Spitzer* at 24 μm. We consider interpretations of the 24 μm emission as originating either from an obscured active nucleus or from star formation and find that the 24 μm detection does not help to uniquely discriminate between the $z = 6.5$ and 2.5 alternatives. We present optical and near-infrared spectroscopy that has, thus far, failed to detect any spectral features. This nondetection helps limit the solution in which the galaxy is a starburst or active galaxy at $z \approx 2.5$, but does not rule it out. If the high-redshift interpretation is correct, HUDF-JD2 is an example of a galaxy that formed by a process strongly resembling traditional models of monolithic collapse, in which a very large mass of stars formed within a remarkably short period of time, at very high redshift.

Subject headings: cosmology: observations — galaxies: formation — galaxies: high-redshift — galaxies: photometry

1. INTRODUCTION

An important goal of observational cosmology is to measure the early history of star formation and stellar mass assembly in galaxies. Such investigations are key elements for testing galaxy formation theories (e.g., Somerville et al. 2001) and the early history of star formation at $z > 6$, providing critical constraints on the time evolution of cosmic reionization (Loeb & Barkana 2001; Stiavelli et al. 2004). Ultraviolet-bright, star-forming Lyman break galaxies (LBGs) have been studied in great detail at $z \sim 3$ and 4 by means of spectroscopic surveys (Steidel et al. 2003), and properties such as their star formation rates, stellar masses, ages, and morphologies have been empirically characterized (see Giavalisco [2002] for a review). Galaxies at $z \approx 2$–3 with redder spectral energy distributions (SEDs) and large stellar masses ($\sim 10^{11}\ M_{\odot}$) have also been identified via infrared surveys (e.g., Franx et al. 2003; Daddi et al. 2004; Yan et al. 2004). A subset of these galaxies appears to be dominated by old stellar populations (e.g., Labbé et al. 2005), suggesting that some high-redshift galaxies formed a large fraction of their stars at substantially higher redshifts, perhaps $z > 5$. Ever increasing numbers of star-forming galaxies at $4 < z \lesssim 6.5$ are being identified in new (mostly optical) surveys, mainly via the Lyman break (Giavalisco et al. 2004a; Ouchi et al. 2004) and narrowband (Rhoads et al. 2004; Ajiki et al. 2004) techniques. The recently acquired Hubble Ultra Deep Field (HUDF) observations, which are the deepest images of the universe at optical and near-infrared wavelengths, have been used to extend color-selected searches to $z > 7$ (Bunker et al. 2004; Yan & Windhorst 2004; Bouwens et al. 2004) and have identified a number of extremely faint candidates that await further studies.

The HUDF is situated within the southern field of the Great Observatories Origins Deep Survey (GOODS; Dickinson & Giavalisco 2003; Giavalisco et al. 2004b). Here we combine the HUDF *Hubble Space Telescope* (*HST*) images at 0.44–1.6 μm

[1] Space Telescope Science Institute, 3700 San Martin Drive, Baltimore MD 21218; b.mobasher@stsci.edu.
[2] Affiliated with the Space Sciences Department of the European Space Agency.
[3] NOAO, 950 North Cherry Avenue, P.O. Box 26732, Tucson, AZ 85726-6732.
[4] Department of Astronomy, Caltech, Mail Stop 105-24, Pasadena, CA 91125.
[5] Johns Hopkins University, 3400 North Charles Street, Baltimore, MD 21218.
[6] Gemini Observatory, Casilla 603, La Serena, Chile.
[7] The Carnegie Observatories, 813 Santa Barbara Street, Pasadena, CA 91101-1292.
[8] Institute fur Astronomie, ETH Zurich, HPF D8 Honggerberg, CH-8099 Zurich, Switzerland.
[9] European Southern Observatory, Karl Schwarzschild Strasse 2, D-85748, Garching bei Munchen, Germany.
[10] INAF, Osservatorio Astronomico di Pavdova, Vicolo dell'Osservatorio 5, I-35122, Padua, Italy.
[11] Space Telescope European Coordinating Facility, European Southern Observatory, Karl Schwarzschild Strasse 2, D-85748, Garching bei Munchen, Germany.
[12] *Spitzer* Science Center, California Institute of Technology, Mail Stop 220-6, Pasadena, CA 91125.
[13] Jet Propulsion Laboratory, California Institute of Technology, Mail Stop 169-506, Pasadena, CA 91109.

with GOODS data in the K_s band (2.16 μm) and data from the *Spitzer Space Telescope* at 3.6–24 μm to search for candidate "*J*-band dropouts," i.e., objects whose light at 1 μm (observed wavelength) is suppressed by the hydrogen opacity of the intergalactic medium (IGM) at $z \gtrsim 7$. We adopt $H_0 = 70$ km s^{-1} Mpc^{-1}, $\Omega_m = 0.3$, and $\Omega_\Lambda = 0.7$ throughout this paper. All magnitudes are in the AB system.

2. IMAGING DATA

The HUDF was imaged at optical wavelengths with the Advanced Camera for Surveys (ACS) Wide Field Camera (WFC), which covers a field of $3' \times 3'$. The images were taken in four passbands: F435W (B_{435}), F606W (V_{606}), F775W (i_{775}), and F850LP (z_{850}). These are the deepest optical images ever obtained, with limiting sensitivity of 29.3–28.5 AB magnitudes in the four filters (10 σ for an extended source measured over a 0.2 arcsec^2 aperture). A detailed description of the HUDF ACS observations and data reduction will be presented in S. V. W. Beckwith et al. (2006, in preparation).

Near-infrared observations of the HUDF were carried out with the Near-Infrared Camera and Multiobject Spectrograph (NICMOS), and cover a field of $2\farcm5 \times 2\farcm5$ with the F110W (J_{110}) and F160W (H_{160}) filters (Thompson et al. 2005). We have used an independent reduction of the HUDF NICMOS data made at STScI (M. Robberto et al. 2006, in preparation), which has slightly reduced noise and has fewer pixel artifacts compared to the version 1 public release data products.[14] The NICMOS images in both bands reach sensitivities of 26.9 AB magnitudes (10 σ in an aperture diameter of $0\farcs6$). GOODS near-infrared data also include a mosaic of K_s-band images from the Very Large Telescope (VLT) Infrared Spectrometer and Array Camera (ISAAC) instrument, which covers the HUDF region with typical exposure times of 6 hr per pointing, seeing FWHM $\approx 0\farcs4$, and limiting sensitivity $K_s = 25.1$ (10 σ point source in a $1''$ diameter aperture; B. Vandame et al. 2006, in preparation; Giavalisco et al. 2004b).

The GOODS Legacy program (M. Dickinson et al. 2006, in preparation) with the *Spitzer Space Telescope* has also surveyed the HUDF using the Infrared Array Camera (IRAC) and the Multiband Imaging Photometer for *Spitzer* (MIPS). The IRAC data consist of images in four bands (3.6, 4.5, 5.8, and 8.0 μm). The HUDF is located in an overlap strip that is covered twice by IRAC in observing epochs separated by 6 months and has therefore received approximately 46 hr of exposure per channel. The formal 10 σ point-source limits range from 25.8 to 23.0 AB mag in the four channels, although in practice, there are measurement errors at the faintest fluxes, which are mainly due to crowding from neighboring objects. The object discussed in this paper is well above the faint-sensitivity limit of the GOODS IRAC images. The MIPS observations at 24 μm have an integration time of approximately 10.4 hr and reach a 5 σ limiting sensitivity of approximately 20 μJy. Source extraction and catalogs for the GOODS 24 μm data will be described in R. Chary et al. (2006, in preparation).

3. IDENTIFICATION AND PHOTOMETRY OF CANDIDATE *J*-BAND DROPOUT GALAXIES

We generated a multiwavelength source catalog based on detections made in the NICMOS F160W band. We used SExtractor (Bertin & Arnout 1996) in dual-image mode with the parameters (kernel, number of connected pixels, and threshold) optimized by means of simulations. These consisted of placing artificial galaxies with known observable parameters in the images and retrieving them following the same procedures used for the real galaxies. We used these catalogs to select very red galaxies with $J_{110} - H_{160} > 1.3$ and no detection (at the 2 σ level) at wavelengths shorter than J_{110}, down to the limit of the ACS/HUDF images (i.e., *J*-band dropouts). The adopted value of $J_{110} - H_{160}$ is the observed color of an LBG with typical rest-frame UV colors, observed at $z = 8$ and taking into account the appropriate cosmic opacity.

Two sources were found that satisfy these criteria: UDF 033242.88−274809.5 and UDF0 33238.74−274839.9 (J2000.0 coordinates). Henceforth, we refer to these objects as HUDF-JD1 and HUDF-JD2, respectively. Both objects are well detected in the ISAAC K_s band and in all four IRAC channels. HUDF-JD2 is clearly resolved in the NICMOS images relative to the point-spread function (PSF); we estimate its half-light radius to be $\simeq 0\farcs30 \pm 0\farcs05$. HUDF-JD1 is more compact, but is probably extended as well. Although HUDF-JD1 satisfies the $J_{110} - H_{160} > 1.3$ color criterion and initially passed the optical nondetection test as well, deeper HUDF/ACS catalogs, generated later, detect faint *z*-band emission at this position. No such optical emission is detected for HUDF-JD2: measurements within an $0\farcs9$ diameter aperture are consistent (within ± 2 σ) with zero flux in all four ACS bands. We also combined the *BViz* ACS images to obtain a white-light image with a 3 σ detection limit of 31.5 mag over a $1\farcs5$ diameter aperture. HUDF-JD2 is still not detected in this combined image, nor is it visible when the combined ACS image is convolved to match the NICMOS PSF.

Both objects were noted previously by Chen & Marzke (2004) and by Yan et al. (2004), using different selection criteria. Prior to the availability of the *Spitzer* data, which, we will demonstrate, is crucial to the interpretation, Chen & Marzke used the NICMOS and ACS data alone and identified these objects as candidates for evolved galaxies with photometric redshifts $z \approx 2.9$ and 4.25, respectively. Yan et al. (2004) used the GOODS IRAC data to identify 17 HUDF objects with extremely red ACS to IRAC colors (IRAC extremely red objects). They estimated $z \approx 3.6$ and 3.4 for the two objects discussed here; however, they considered the photometric redshifts and stellar population modeling to be uncertain due to the lack of any optical detection and therefore excluded these two objects from the detailed analysis of their sample.

The observed SED of HUDF-JD1 rises smoothly longward of the *J* band, in contrast to the HUDF-JD2 SED, which is almost flat in the *H*/*K* region (i.e., a blue $H - K$ color), followed by a significant break in between the K_s and 3.6 μm wavelengths (i.e., a red $K - 3.6$ color). We argue below that this distinctive feature, seen only in HUDF-J2, is strong evidence for a high-redshift galaxy ($z \sim 7$). By contrast, the smooth SED of HUDF-JD1 is consistent with a dusty poststarburst at $z = 2.4$ with $E(B - V) = 0.8$, an age of 200 Myr, and metallicity $Z = 0.008$. The two sources differ in other respects. X-ray observations of the GOODS-S field (the 1 Ms X-ray survey) with the *Chandra X-Ray Observatory* (Giacconi et al. 2002) shows HUDF-JD1 to be coincident (within $1''$) with a faint X-ray source (D. Alexander 2004, private communication, based on an extension of the faint supplemental X-ray catalog from Alexander et al. 2003). HUDF-JD2, instead, has no significant X-ray detection, with 3 σ upper limits of 5.1×10^{-17} and 2.4×10^{-16} ergs s^2 cm^{-2} in the soft (0.5–2 keV) and hard (2–8 keV) bands, respectively. For the remainder of this paper, we concentrate on interpreting HUDF-JD2. Images of HUDF-JD2 from 0.44 to 8.0 μm are shown in Figure 1.

[14] These have since been replaced by improved version 2 NICMOS data products.

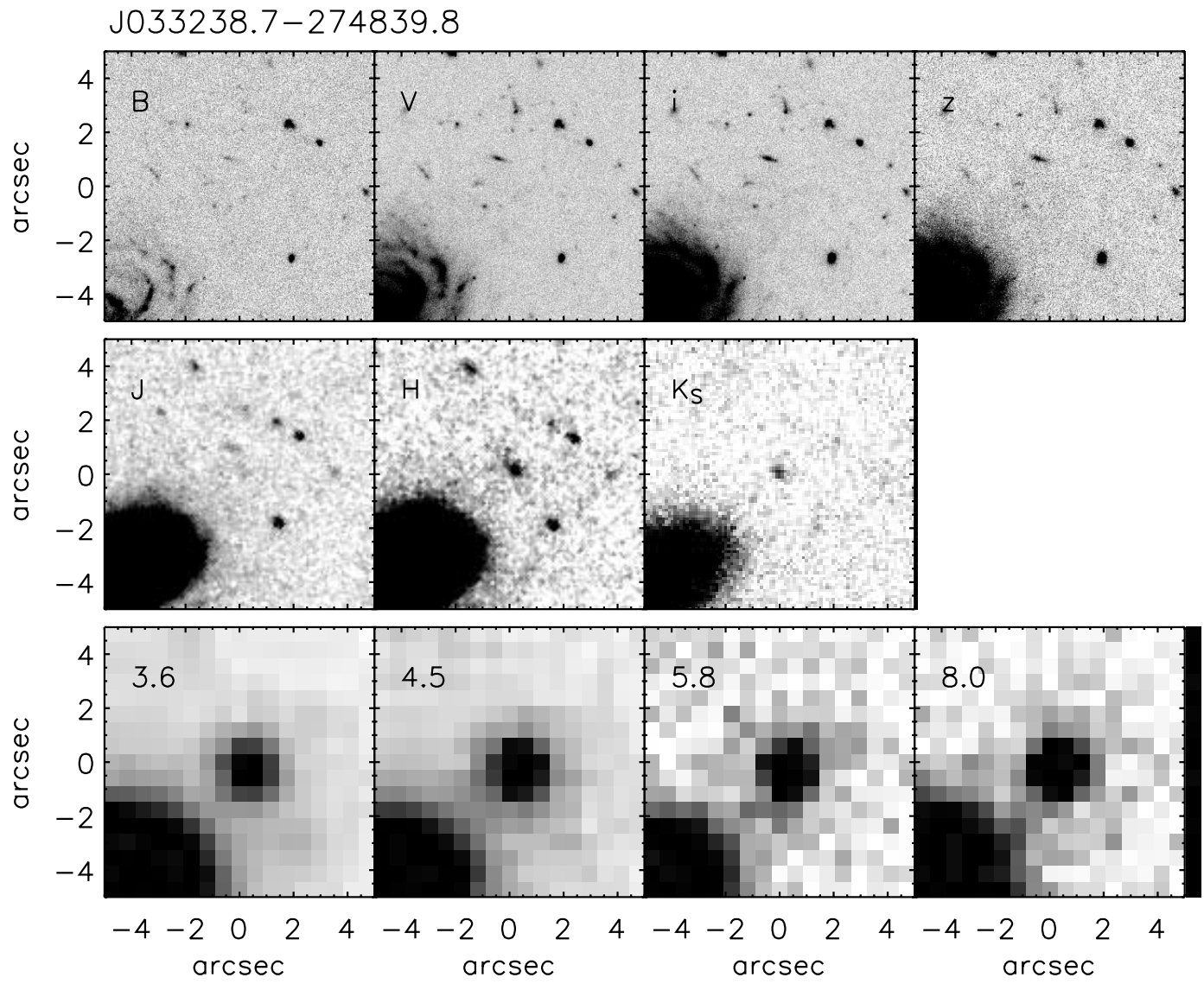

FIG. 1.—Images of the *J*-dropout candidate HUDF-JD2 ($\alpha = 3^{h}32^{m}38^{s}.74$; $\delta = -27^{\circ}48'39''.9$, J2000.0) from *HST* ACS (B_{435}, V_{606}, i_{775}, and z_{850}), *HST* NICMOS (J_{110} and H_{160}), VLT ISAAC (K_s), and *Spitzer* IRAC (3.6–8.0 μm). The K_s ISAAC image is from deep FIRES (Faint Infrared Extragalactic Survey) observations.

We carefully remeasured photometry for HUDF-JD2 in each imaging data set through a variety of apertures, using different sky background estimates, and paying close attention to the possible contaminating effects of nearby neighbors. There are three faint blue objects, visible at wavelengths as short as the ACS B_{435} band, located slightly more than $1''$ from the H_{160}-band centroid of HUDF-JD2. For large photometric apertures, these neighbors significantly affect measurements in the NICMOS J_{110} band or in ACS, but they have relatively small effects in the H_{160} band and at longer wavelengths. We have masked circular regions with diameter $0''.5$ around each of these sources before measuring photometry in the NICMOS and ISAAC images and use a smaller aperture, which excludes them in ACS.

A portion of the SED of HUDF-JD2 that features prominently in our later discussion is the break seen between the K_s and 3.6 μm IRAC bands. Since the signal-to-noise ratio (S/N) in the GOODS ISAAC K_s-band image is less than that in the NICMOS H_{160} or IRAC images, it is important to verify that this is not an artifact due to measurement error. Here we use a deeper (14 hr exposure time) VLT ISAAC K_s-band image of the HUDF (I. Labbé et al. 2006, in preparation). We calibrated the photometric zero point of the deeper image to that of the GOODS K_s-band data by comparing measurements for eight galaxies common to the two images. Photometry was then repeated on the deep K_s image, and we found excellent agreement with the measurement from the GOODS images within the nominal photometric uncertainties of the two data sets. Because of its higher S/N, we use the K_s measurements from the deeper image here.

We measured the *JHK*-band magnitudes through circular apertures with diameters as large as $3''$ and found that the photometric curve of growth converges to a diameter of $2''$. We examined the dependence of aperture magnitudes on different prescriptions for sky subtraction (concentric annuli or median of the data in a local region) and found that for aperture diameters of $2''$ and smaller, these did not affect the measurements at a level greater than our estimates for the photometric uncertainty due to background shot noise. For the *JHK* photometry, we choose $2''$ aperture diameters as a trade-off between convergence of the total flux, the net S/N, and the effects of systematic uncertainty in the background subtraction. We also verified the large-aperture $J_{110} - H_{160}$ and $H_{160} - K_s$ colors by comparing them to measurements through a smaller ($0''.9$ diameter) aperture using versions of the NICMOS images that

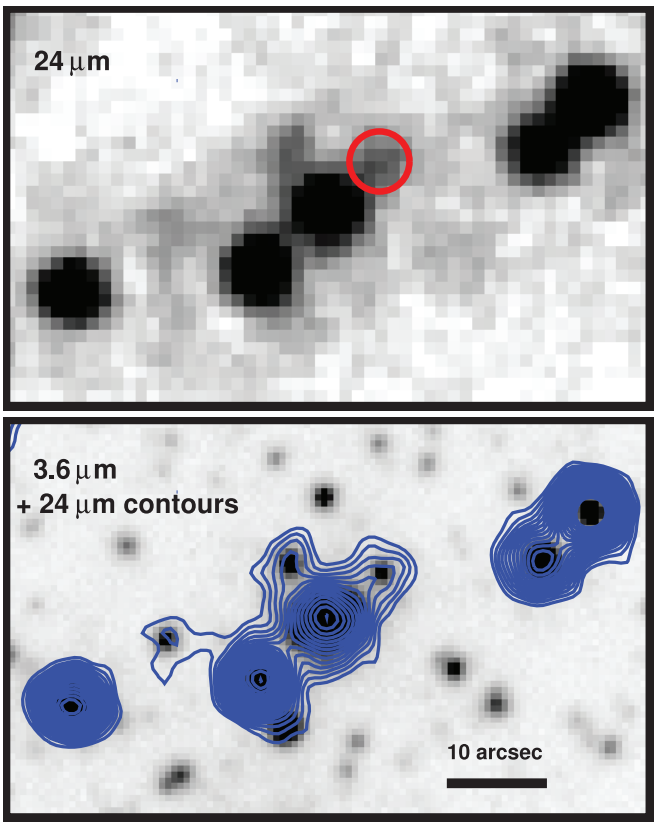

FIG. 2.—*Top*: MIPS 24 μm image of the region around HUDF-JD2. The position of the source as measured from the NICMOS H_{160} image is marked by the red circle, which has a diameter of 6″, approximately the FWHM of the 24 μm PSF. *Bottom*: IRAC 3.6 μm image, with contours from the 24 μm superposed.

were carefully convolved to match the PSF of the ISAAC K_s image using a kernel derived by Fourier techniques. The small-aperture measurements have higher S/N and are less subject to sky-subtraction errors, and the results were in excellent agreement with the large-aperture values within the estimated uncertainties. Final photometric errors were computed from the sky noise, including corrections for pixel correlations induced by the reduction process, with an additional term representing shot noise uncertainty on the net sky background.

Photometry in the ACS *BViz* images was measured through 0.″9 diameter apertures centered at the position of HUDF-JD2 derived from the NICMOS H_{160}-band image, and uncertainties were estimated based on the background shot noise (which is uncorrelated in the ACS HUDF data). The object is undetected (with S/N < 2) in all bands.

The IRAC photometry was measured with SExtractor using 4″ diameter circular apertures and transformed to total magnitudes using aperture corrections based on Monte Carlo simulations in which artificial images of compact galaxies (half-light radii $\leq$0.″5, appropriate for this object) were added to the IRAC images after convolution by the appropriate PSF and recovered by SExtractor. The results were the same within the expected errors when using smaller (3″diameter) circular apertures or SExtractor MAG_AUTO measurements. The three faint galaxies close to HUDF-JD2 lie within the aperture used for IRAC photometry. However, these are expected to be too blue to make any substantial contribution to our estimated IRAC magnitudes. The baseline IRAC photometric errors were estimated from the same simulations in order to take into account the statistical effects of crowding in the data. The errors from the simulations ranged from 0.06 to 0.11 mag in the four channels. In practice, we set a floor to the IRAC errors of 0.10 mag in channels 1–3 and 0.15 mag in channel 4 to also account for remaining uncertainties in the IRAC photometric calibration.

HUDF-JD2 is also detected in the 24 μm MIPS image, as illustrated in Figure 2. Emission from the foreground spiral galaxy 7.″3 to the southeast makes it necessary to carefully deblend the two objects. We have done this in two independent ways, using two independent reductions of the MIPS image. In one case, we fit point sources to the 24 μm data at positions defined by the presence of sources in the higher resolution IRAC images. We calculate the photometric uncertainties by quadrature summation over the residuals after the point-source fits are subtracted. In this way, we measure a 24 μm flux density of 51.4 $\pm$ 4.0 μJy. We also measured photometry through small circular apertures centered at the position of the IRAC counterpart to HUDF-JD2, applying corrections to total flux computed from an in-flight 24 μm PSF available from the *Spitzer* Science Center. The smallest aperture that we used (4″ diameter) minimizes contamination from the neighboring spiral, but requires the largest aperture correction (a factor of 4.8). This yielded a flux density of 60 $\pm$ 5.0 μJy, while larger apertures were brighter, indicating increasing contributions from the neighboring spiral. We adopt the PSF-fitting flux, but increase the uncertainty estimate to 20% (10 μJy) to reflect the difficulty of deblending these sources and to encompass the range of values measured by the different techniques. The MIPS cataloging procedure will be presented in detail in R. Chary et al. (2006, in preparation).

The photometric data used to construct the SED discussed in § 4 are presented in Table 1. The difference between the NICMOS (*JH*) and IRAC (8 μm) HUDF-JD2 magnitudes in Table 1 and those presented in Yan et al. (2004) is mainly due to using differently reduced

TABLE 1
PHOTOMETRY FOR *J*- DROPOUT CANDIDATE HUDF-JD2

Parameter	Value
B_{435}	>30.61
V_{606}	>31.02
i_{775}	>30.88
z_{850}	>30.26
J_{110}	27.02 ± 0.32
H_{160}	24.94 ± 0.07
K_s	23.95 ± 0.13
$m_{3.6}$	22.09 ± 0.10
$m_{4.5}$	21.80 ± 0.10
$m_{5.8}$	21.60 ± 0.10
$m_{8.0}$	21.38 ± 0.15
m_{24}	19.63 ± 0.21

NOTES.—Coordinates are R.A. 53.161425, decl. −27.81107 (J2000.0). Magnitudes, followed by their associated errors, are in the AB system. *HST* ACS magnitudes are given as 2 σ upper limits.

NICMOS images, removing the three nearby faint sources and the bright foreground galaxy in the field of HUDF-JD2, and applying a different photometric procedure in the case of the IRAC data.

4. SPECTRAL ENERGY DISTRIBUTION AND STELLAR POPULATION MODELING

The spectral energy distribution (SED) of HUDF-JD2 is presented in Figure 3; the ACS measurements are shown as 2 σ upper limits. The SED displays a significant change of slope between the measurements in the mid-infrared (3.6–8 μm) wavelength range and those in the near-infrared (1.1–2.2 μm). This change of slope is punctuated by a break observed between the K_s and 3.6 μm points mentioned earlier. The SED declines shortward of 1.6 μm and is undetected in the HUDF ACS images. At the longest wavelengths, there is another change of slope in the SED between the IRAC and MIPS bands, with an upturn at $\lambda >$ 8 μm (see Fig. 6).

As we show in § 4.1, the photometry of HUDF-JD2 at wavelengths shorter than 8 μm can be modeled as emission from an evolved stellar population seen at $z \approx 6.5$. The main evidence for this is the observed $K_s - 3.6$ μm break, which is interpreted as the λ_0 3646 Å Balmer break from an established stellar population. We also consider old or dust-reddened stellar population models at lower redshifts. These models are illustrated by the spectra overplotted in Figure 3. In any scenario, the measured 24 μm flux density exceeds that predicted by the stellar population models alone by more than an order of magnitude. This and the distinct change of SED slope between the IRAC and MIPS bands strongly suggest that the 24 μm emission from HUDF-JD2 results from a different physical mechanism than that responsible for the bulk of the light at wavelengths shorter than 8 μm. This may arise from warm dust or complex molecules such as polycyclic aromatic hydrocarbons (PAHs), or it may be a highly dust-reddened continuum source. We will therefore separately model the data at $\lambda \leq 8$ μm (§§ 4.1 and 4.2) and at 24 μm (§ 4.3). Any solution must provide an acceptable explanation for the 24 μm flux without invalidating the fits obtained for shorter wavelengths.

4.1. *Stellar Population Modeling*

We now perform detailed modeling of the observed HUDF-JD2 SED in the range $\lambda \leq 8$ μm, over which the flux is dominated by a stellar component. We used two evolutionary synthesis codes in order to model the observed SED: Starburst99 (Leitherer et al. 1999 Vázquez & Leitherer 2005) and Bruzual & Charlot models (2003, hereafter BC03). The Starburst99 code has recently been extended to follow stellar populations to ages ~5 Gyr (Vázquez & Leitherer 2005). Starburst99 only supplies instantaneous and continuous star formation modes. For the BC03, we used models with exponentially decreasing star formation rates parameterized by a timescale τ. A model with $\tau = 0$ is thus identical to the instantaneous star formation in the Starburst99 models. For all models we used a Salpeter initial mass function (IMF) with a lower and upper mass cutoff at 0.1 and 100 $M_\odot$, respectively.

We searched for the best model fit to the observed data by simultaneously optimizing the parameters of redshift (z), extinction [$E(B-V)$], starburst age (t_{sb}), and metallicity (Z). The continuous star formation mode in the Starburst99 models could not produce an SED even remotely resembling the observed one and was not considered further. In the case of the BC03 models we also include the e-folding timescale for a decreasing star formation rate (τ). The best-fit parameters were found through χ^2 minimization (with 2 degrees of freedom; 7 data points and 5 parameters to fit), where we allowed all possible combinations of model parameters in the ranges $0 < z < 10$, $0 < E(B-V) < 1$, and $0.1 < t_{sb} < 2.4$ Gyr and four levels of metallicity, $Z =$ 0.004, 0.008, 0.02, and 0.05. For the BC03 models we used $\tau = 0$, 100, 200, 300, 400, 600, 800, and 1000 Myr. We used the Madau (1995) prescription for the mean neutral hydrogen opacity of the IGM and modeled dust extinction as a foreground obscuration screen at the redshift of the galaxy using the obscuration law of Calzetti et al. (2000). As we will see, however, the best-fitting models have little or no dust extinction, so the choice of prescription for the reddening makes little difference in the final results.

The parameters of the best-fit models using the two different evolutionary synthesis codes are summarized in Table 2. The results are very similar for both the Starburst99 and BC03 models, and we plot the best-fit result from BC03 in Figure 3, together with the observed photometry.

When fitting broadband colors, there are degeneracies between parameters such as age, metallicity, extinction, and redshift. However, with seven significant photometric detections plus four upper limits, we find that there are sufficient data to limit most of these degeneracies. In Figure 4, we plot (as a gray scale) the minimum χ^2_ν as a function of redshift and extinction, after marginalizing over the other free parameters. The global χ^2_ν minimum is marked by an asterisk at $z = 6.6$ and 6.5 for the Starburst99 and BC03 models, respectively, and $E(B-V) = 0$ for both sets of models. The best-fitting redshifts are comparable to those of the most distant galaxies now known, although we note that the region of acceptable χ^2_ν values is skewed toward still larger redshifts. The parameters not explicitly shown in Figures 4, such as starburst age and metallicity, do not vary much over the region defined by the 95.4% confidence level. Hence, only a small number of parameter combinations actually produce good fits of the model SED, and the redshift turns out to be quite robustly constrained, as also shown through Monte Carlo simulations (§ 4.2). The stellar mass of the best-fitting models lies in the range $M_* = (5\text{–}7) \times 10^{11}$ $M_\odot$. This represents a remarkably large mass for a high-redshift galaxy, and we consider its implications in some detail in § 6.

The metallicity of HUDF-JD2 is not strongly constrained by the modeling. This can be seen by the fact that the BC03 and Starburst99 models yield different values for the metallicity, although most other derived parameters are very similar (Table 2). Moreover, given the low metallicity ($Z = 0.004$) predicted by

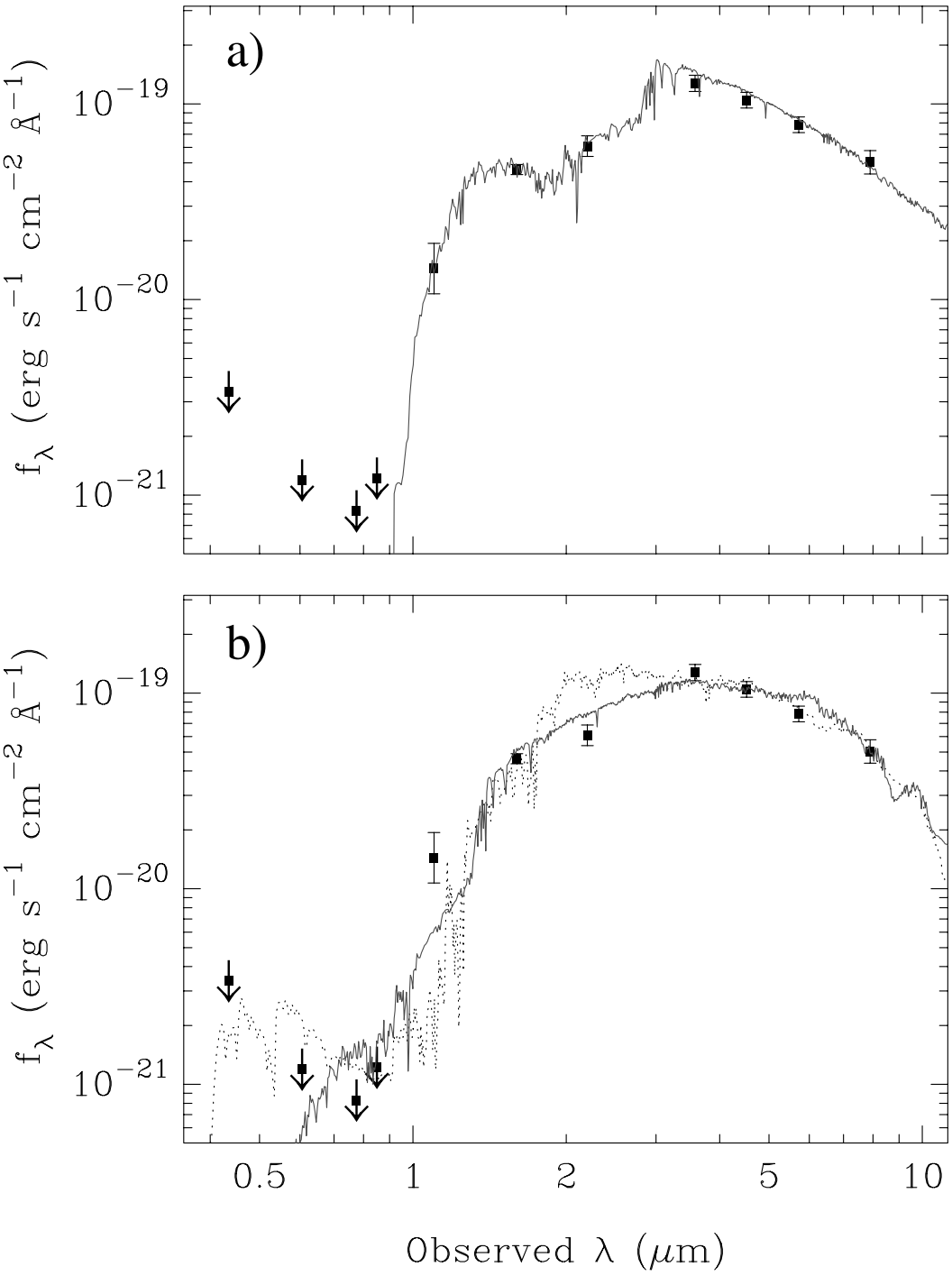

FIG. 3.—Observed and model SED of HUDF-JD2. (*a*) Model SED based on the best-fit BC03 model (*solid line*; see Table 2) at a redshift $z = 6.5$. (*b*) Alternative, lower redshift models. The solid line shows the best fit for a dusty model galaxy at $z = 2.5$, the best fit from the secondary χ^2 minimum seen in Fig. 4. The parameter values are given in Table 2. The dotted line shows the SED for an old population with $z = 3.4$ and an age of 2.4 Gyr (Table 2).

the BC03 model, no gas, and a high mass ($\sim 5 \times 10^{11}\ M_\odot$), the object does not lie on any known mass-metallicity relation. To further explore this, we fix metallicity to a relatively high value of $Z = 0.02$ (solar) and perform the fit to optimize the other parameters. The best fit gives $z = 6.5$, $E(B - V) = 0.0$, $t_{\rm sb} = 600$ Myr, and $\tau = 0$, with $\chi^2_\nu = 2.3$. Acceptable fits can also be found for $t_{\rm sb} = 500$ Myr combined with small amount of extinction [$E(B - V) \sim 0.03$–0.05]. As the age becomes progressively younger (<500 Myr), there is an increased need for higher extinction, with χ^2_ν becoming monotonically worse. This is further confirmed by our Monte Carlo simulation results presented in § 4.2.

Figure 4 suggests that a dusty galaxy at $z \approx 2.5$ also provides a possible, although less likely, alternative fit to the data. The best-fit parameters corresponding to this model are also listed in Table 2, and the model is compared to the observed photometry in Figure 3*b*. In order not to violate the very stringent ACS detection limits, this dusty model must also be a poststarburst object, without ongoing star formation. A foreground dust screen obeying the Calzetti et al. (2000) attenuation law cannot adequately

TABLE 2
PARAMETERS FOR THE BEST-FIT MODELS TO HUDF-JD2

Parameter	Starburst99[a]	BC03[b]	Dusty[c] $z < 4$	Old[d] $z < 4$
z	6.6	6.5	2.50	3.4
$E(E-B)$	0.0	0.0	0.70	0.0
Z	0.020	0.004	0.020	0.050
t_{sb} (Gyr)	1.0	1.0	0.6	2.4
τ (Myr)	...	0	0	0
L_{bol} ($L_\odot$)	1.0×10^{12}	1.0×10^{12}	3.5×10^{11}	2.1×10^{11}
M_*/L_{bol} ($M_\odot/L_\odot$)[e]	0.71	0.42	0.29	0.95
M_* ($M_\odot$)[f]	7×10^{11}	5×10^{11}	1×10^{11}	2×10^{11}
z_{form}[g]	>9	>9	...	...
χ^2_ν[h]	1.8	1.9	6.7	29.9

[a] Starburst99 ver. 5.0 (Vásquez & Leitherer 2005).
[b] Bruzual & Charlot (2003).
[c] Best-fit parameters forcing $z < 4$.
[d] Best-fit parameters forcing $z < 4$ and $E(B - V) = 0$.
[e] Stellar mass loss is included in the ratio.
[f] Salpeter IMF with lower and upper mass cutoff at 0.1 and 100 $M_\odot$.
[g] The 95% lower confidence limit based on high-redshift ($z > 1$) solution from Monte Carlo simulations.
[h] χ^2 per degree of freedom ($\nu = 2$).

suppress the UV flux from active star formation while simultaneously matching the near-infrared and IRAC photometry, although we note that steeper UV extinction laws might be able to accomplish this. If the 24 μm flux from HUDF-JD2 is due to the presence of active star formation and not an active galactic nucleus (AGN), then this may appear to contradict the poststarburst nature of the fit to the ACS through IRAC SED. However, more complex models with a highly obscured starburst or active nucleus plus a more lightly obscured, non–star-forming host galaxy could conceivably fit the data. Table 2 also gives parameters for another alternative model, which represents an unreddened, passively evolving older stellar population at $z = 3.4$. This gives a still worse fit to the data, poorly matching the break from the near-infrared to IRAC photometry and violating the optical non-detection limits in some ACS bands. A similar model dominated by old stellar populations was also used by Yan et al. (2004), deriving the same redshift of $z = 3.4$ for the HUDF-JD2. However, this substantially overpredicts the observed K-band flux of the object and seems very unlikely.

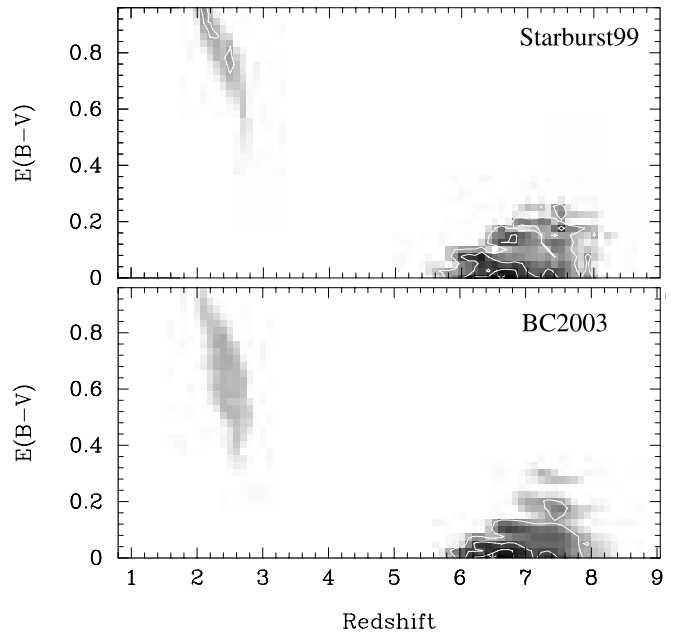

FIG. 4.—Reduced χ^2 values of the best-fitting models as a function of redshift z and extinction $E(B-V)$, shown as gray scale, for Starburst99 (*top*) and BC03 models (*bottom*). Black corresponds to the lowest χ^2 value, ~1.9, and white to $\chi^2 > 10$. The contours show the 68%, 90%, and 95.4% confidence of the χ^2 fit, and the white asterisks mark the best-fitting solutions.

4.2. *Monte Carlo Simulations*

To test the stability of the parameter values from the model fitting and to better understand the relative likelihoods of the high- and low-redshift interpretations of HUDF-JD2, we have carried out Monte Carlo simulations, simultaneously varying the fluxes in all bands under the assumption that their errors are normally distributed and uncorrelated. We generated 1000 realizations of the data and fit each, using the BC03 models. The distribution of the fitted values defines a probability distribution for each parameter and is a better assessment of the most likely values. In Figure 5 we show the probability distributions for the redshift, stellar mass, extinction, and formation redshift (z_{form}) values. The z_{form} is calculated from the estimated photometric redshift and the age of the stellar population (t_{sb}) in HUDF-JD2, using the cosmology adopted here. The redshift distribution shows the same behavior depicted in Figure 4, with a median probability around $z \sim 6.9$, but skewed to somewhat higher redshift. As before, a less prominent peak is evident at $z = 2$–3, corresponding to a dust-obscured solution. In each panel of Figure 5, the parameter histograms corresponding to the low-redshift ($z < 4$) and high-redshift ($z > 4$) solutions are shaded differently so that the properties of each family of solutions can be easily distinguished. The distribution for extinction is strongly peaked at $E(B - V) \approx 0.0$, with a small number of high values corresponding to the low-redshift solutions. For the high-redshift solutions, the distribution of stellar mass peaks around $5 \times 10^{11}\ M_\odot$, as for the best-fit model. The starburst age (not shown in Fig. 5) is evenly spread between ~0.4 and 1.0 Gyr, where the upper limit corresponds to the best-fit solution in § 4.1. The e-folding time is confined to 0.0 and 100 Myr, i.e., short compared to the ages of the models, while the preferred metallicity is 0.004–0.008. Considering only the high-redshift ($z > 5$) solutions, 95% of the Monte Carlo realizations have $z_{form} > 9$, while 53% have $9 < z_{form} < 20$; 14% of models exceed the age of the universe at their best-fitting photometric redshifts and hence are unphysical.

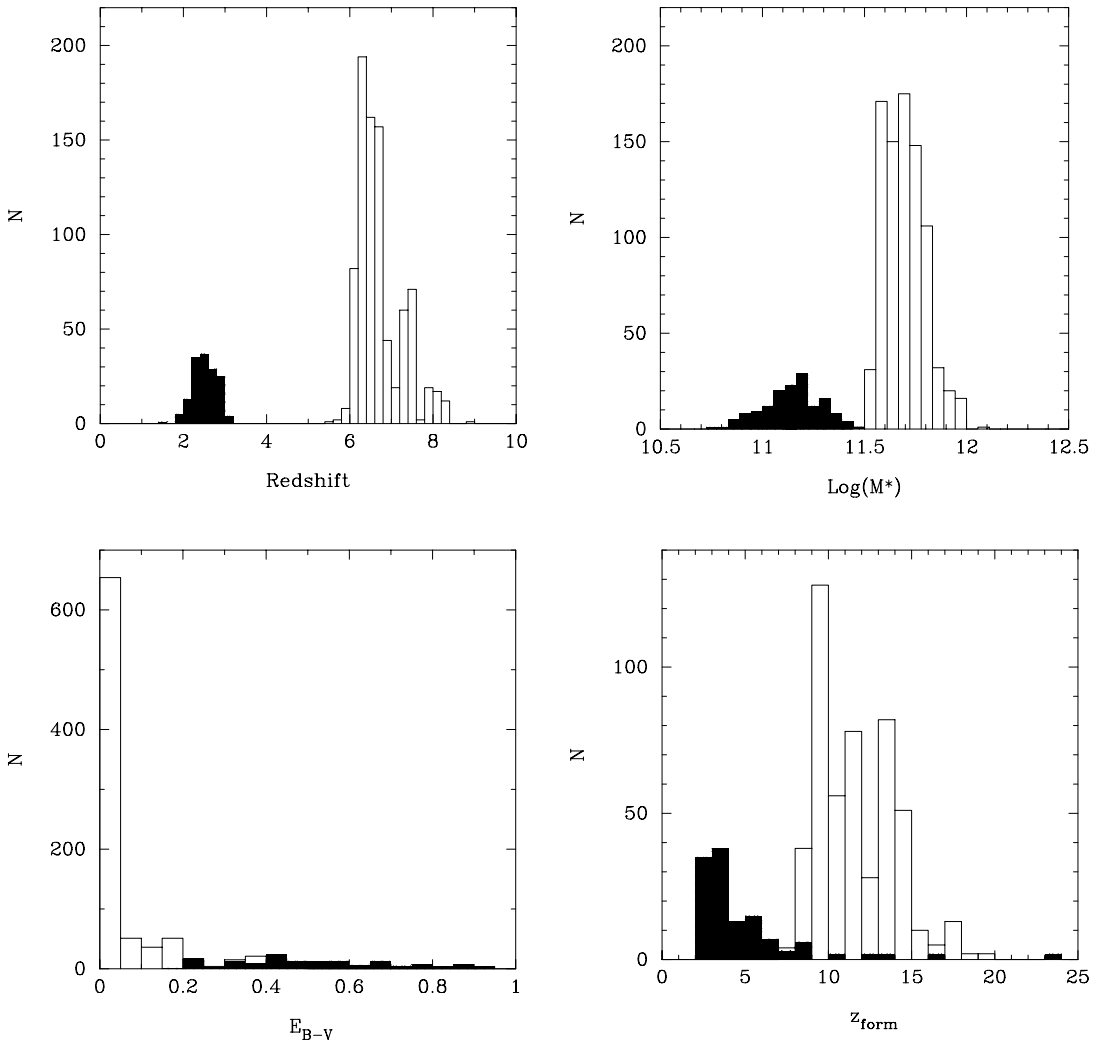

FIG. 5.—Results from Monte Carlo simulations in which the photometric measurements of HUDF-JD2 in all bands were allowed to vary simultaneously according to their estimated errors. The panels show the distribution of parameter values for the best-fitting BC03 models fit to each Monte Carlo realization. *Top left*, Redshift; *top right*, stellar mass (in solar units); *bottom left*, extinction $E(B-V)$; *bottom right*, formation redshift $z_{\rm form}$, where realizations for which the formation redshift is in conflict with the age of the universe have been removed. Dark histograms correspond to the alternative dusty solution at $z \sim 2.5$.

The relatively narrow distributions for key parameters show that the stellar population model fits are stable and are not greatly affected by the photometric uncertainties. In particular, the redshift is one of the more robust parameters. Age and extinction vary only by small amounts, and most of the best-fitting models have relatively small amounts of ongoing star formation, i.e., with age $t_{\rm sb} \gg \tau$. Old stellar populations at $z < 4.5$ do not fit the data well. Dusty, poststarburst models at $z \approx 2$–3 provide relatively poor fits to the observed data, outside the 95.4% confidence range, but do populate a minority of the solutions in the Monte Carlo simulations when the photometry is allowed to vary within its nominal range of errors.

In summary, therefore, Figures 4 and 5 suggest that the HUDF-JD2 is likely to be an extremely massive galaxy observed at $6 < z < 8$ that formed the bulk of its stars at $z_{\rm form} > 9$. The size of the observed $K_s - 3.6$ μm break implies a poststarburst system now being observed in a quiescent state. The fraction of realizations in Figure 5, leading to low-z ($z < 5$) and high-z ($z > 5$) solutions over the entire χ^2 range, are found to be 15% and 85%, respectively, as estimated from Monte Carlo simulations, with no strong dependence on the explored χ^2 range.

4.3. *Interpreting the* 24 μm *Emission*

We now consider the 24 μm upturn in the SED in the context of the stellar population models discussed in the previous subsections. For either of the two classes of solutions ($z \sim 6.5$ or 2.5), the 24 μm emission could be due to the presence of dust heated by star formation or by an AGN.

For the $z \approx 6.5$ scenario, we regard the AGN hypothesis as more likely. At that redshift, the MIPS 24 μm band samples rest-frame wavelengths of $\sim$3.2 μm. Although there is a relatively weak PAH emission band at this wavelength, the SEDs of star-forming galaxies typically reach a local minimum at roughly this wavelength, between the Rayleigh-Jeans portion of the stellar photospheres and the mid-infrared emission from warm dust and PAHs. Instead, dust-obscured AGNs can be much brighter in these wavelengths, due to the presence of a substantially warmer dust component heated by the active nucleus. The reddened continuum from the nucleus itself can also contribute to the emission at these wavelengths. Moreover, we have inferred that HUDF-JD2 is an exceptionally massive galaxy if it is indeed at $z \approx 6.5$. If the relation between bulge mass and black hole mass, found

locally, holds at high redshift, then we might expect HUDF-JD2 to host a supermassive black hole at its core.

Although there is no unique prescription for the near- to mid-infrared SED of AGNs, we illustrate two possible scenarios here based on the properties of nearby infrared-luminous AGNs, namely, Mrk 231 and NGC 1068. The former is an ultraluminous infrared source, optically classified as a broad absorption-line QSO with an active nucleus bright at optical through mid-infrared wavelengths. The latter, instead, is the prototypical Seyfert 2 galaxy, whose active nucleus is highly obscured at optical and near-infrared wavelengths. We compiled photometry for both objects using the NASA Extragalactic Database. Mrk 231 is more distant (178 Mpc) than NGC 1068 (16 Mpc), and most of the available photometry covers larger apertures (10″–15″ diameter), encompassing light from both the active nucleus and the host galaxy. Therefore, there is probably some stellar component to the reported Mrk 231 photometry that we use here; a hint of this can be seen in a bump in its SED at rest-frame $\lambda \approx 1.6$ μm, which is a characteristic feature of starlight. For NGC 1068, we use the smallest aperture nuclear data available, compiled by Galliano et al. (2003), and have spliced in an ISOPHOT-S spectrum at 5.8–11.6 μm, whose intensity we have rescaled to match that of the small-aperture photometry in the overlapping wavelength range of 7.7–10.4 μm. This, therefore, is our best approximation to the nuclear spectrum of a highly reddened AGN in the rest-frame wavelength range 1–10 μm. We shift both AGN templates to $z = 6.5$ and scale them to match the measured 24 μm flux of HUDF-JD2. For our adopted cosmology, this required multiplying Mrk 231 by a factor of 2.85, while the NGC 1068 nuclear template was multiplied by a factor of 105. Figure 6*a* shows these two AGN models overplotted with the photometric data and the best-fitting $z = 6.5$ BC03 model from Table 2 and Figure 3*a*.

Both AGN models provide a long-wavelength upturn over the stellar SED for HUDF-JD2. The NGC 1068 nucleus is very heavily reddened and would contribute negligibly to the flux of HUDF-JD2 at any observed wavelength shorter than 10 μm. For the rescaled Mrk 231 template, the contribution to the observed IRAC fluxes for JD2 ranges from 25% at 3.6 μm to 53% at 8.0 μm. However, we reiterate that the SED adopted here for Mrk 231 most likely includes some component of the stellar host galaxy. At wavelengths shorter than 3 μm, where the flux from HUDF-JD2 drops sharply below the break, the fractional contribution from the AGN becomes larger again, although we do not have rest-frame UV photometry of Mrk 231 suitable for extending this comparison across the whole observed wavelength range.

If an active nucleus contributes some fraction of the light seen at observed 1–8 μm wavelengths, this might reduce the implied stellar mass and possibly change other derived stellar population properties. Assuming that the AGN spectral energy distribution is like that of the Mrk 231 template and that it contributes negligibly at shorter wavelengths, we subtract the AGN contribution (which is presumed to produce all of the observed 24 μm emission) from the observed fluxes from the K_s band to 8 μm and repeat the χ^2 fitting as before. As a result, we derive a somewhat higher redshift ($z = 7.2$) and a stellar mass that is reduced by a factor of 2. This is mainly due to the enhanced strength of the $K_s - m(3.6\ \mu\text{m})$ break, although we note that this depends in detail on the behavior of the adopted AGN template in the rest-frame UV. If instead the AGN contribution to the 24 μm emission is represented by the rescaled NGC 1068 nuclear template, it would contribute no significant amount of light to fluxes at the observed 1–8 μm wavelengths, and correspondingly there would be no change in the derived stellar population properties of the host galaxy.

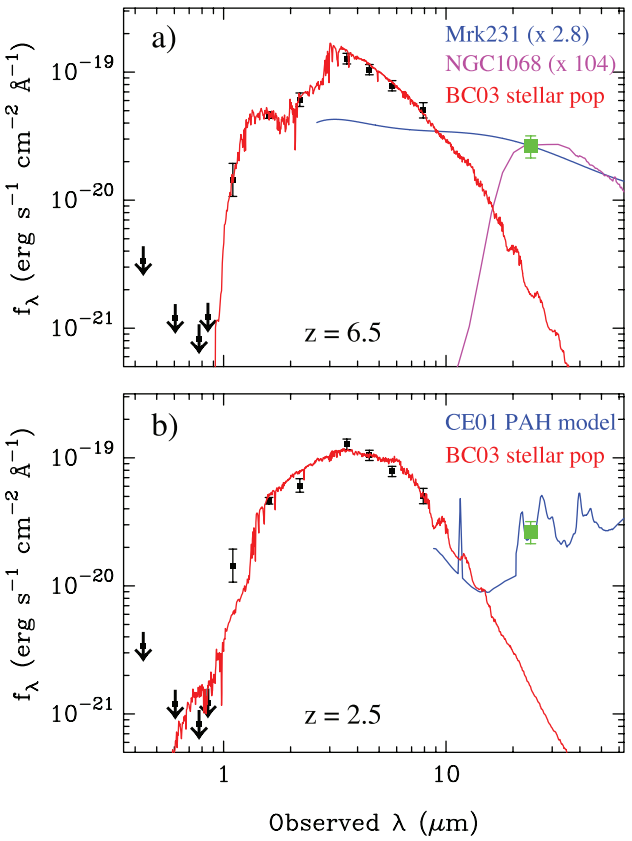

FIG. 6.—Observed and model spectral SEDs for HUDF-JD2, extended to include the 24 μm measurement. The models that best fit the data at $\lambda \leq 8$ μm (see Fig. 3; Table 2) are shown as red lines in both panels. (*a*) Solution for $z = 6.5$. Two models of obscured, infrared-luminous AGNs are shown, normalized to the observed 24 μm point: the ultraluminous infrared AGN Mrk 231, scaled in luminosity by a factor of 2.85, and the highly obscured Seyfert 2 nucleus NGC 1068, scaled by a factor of 105. (*b*) Solution for $z = 2.5$. A model starburst galaxy template from CE01, with $L_{\rm IR} = 2 \times 10^{12}$ $L_\odot$, is shown, normalized to the 24 μm photometry.

AGNs commonly emit X-rays, but HUDF-JD2 is undetected in the 1 Ms *Chandra* GOODS-S data. The nuclear X-ray emission from both Mrk 231 and NGC 1068 are believed to be absorbed by a Compton-thick screen of neutral gas. Braito et al. (2004) have directly detected the unabsorbed X-ray emission from Mrk 231 at energies up to 60 keV. They derive a neutral column density $N(\text{H I}) = 2 \times 10^{24}$ cm^{-2} and infer an intrinsic (unabsorbed) 2–10 keV luminosity of $0.5–2.0 \times 10^{44}$ ergs s^{-2}. For a source at $z = 6.5$, the *Chandra* hard band (2–8 keV) is sensitive to rest-frame energies 15–60 keV, where Mrk 231 would be less heavily absorbed. Extrapolating the luminosity derived by Braito et al. with a power-law spectrum with photon index $\Gamma = 1.7$ (where $dn/dE \propto E^{-\Gamma}$) and multiplying the luminosity of Mrk 231 by a factor of 2.85 as was done to match the 24 μm photometry, we would predict an X-ray flux of $(4.5–18) \times 10^{-16}$ ergs s^{-1} in the *Chandra* 2–8 keV band. This is 1.9–7.5 times larger than the 3 σ hard-band detection limits. However, AGNs may span a broad range of mid-infrared to X-ray flux ratios, depending on their degree of obscuration. Matt et al. (2000) find that the direct X-ray emission from the NGC 1068 nucleus is completely absorbed at all energies out to 100 keV by an absorbing column density $N(\text{H I}) > 10^{25}$ cm^{-2}. Only a reflected component of nuclear X-ray emission is detected, about 2 orders of magnitude fainter than the intrinsic nuclear luminosity. X-rays from a high-redshift AGN of this type would therefore be undetectable with *Chandra*.

In the $z \approx 2.5$ hypothesis, the MIPS 24 μm band samples the rest frame at $\sim$7 μm, where there are strong complexes of PAH emission. Both starburst and AGN scenarios are plausible at this redshift. However, the absence of detectable X-ray emission from HUDF-JD2 leads us to concentrate on the starburst interpretation here, although again a Compton-thick AGN cannot easily be ruled out. Indeed, Reddy & Steidel et al. (2004) and Donley et al. (2005) have shown examples of broad-line or radio-detected AGNs in GOODS-N that are faint or undetected in the 2 Ms *Chandra* X-ray data. Figure 6*b* shows the previous best-fit $z \sim 2.5$ solution, a dusty poststarburst spectrum, superposed with an infrared spectral template from Chary & Elbaz (2001, hereafter CE01), normalized to match the 24 μm measurement. The model is an ultraluminous infrared galaxy (ULIRG) with $L(8-1000\ \mu\mathrm{m}) = 2 \times 10^{12}\ L_{\odot}$. The CE01 templates include a stellar host galaxy component that dominates the emission at rest-frame wavelengths shorter than about 4 μm, which we neglect here because we model the starlight independently. The warm dust and PAH emission from the starburst have no significant effect on the photometry in the IRAC bands or at shorter wavelengths.

In summary, we conclude that the 24 μm emission from HUDF-JD2 can be interpreted under either the $z \approx 6.5$ or 2.5 scenarios and cannot be used as a diagnostic to clearly discriminate between these alternatives. At high redshift, a luminous but highly obscured AGN (a type II QSO) is the favored interpretation, while at $z \approx 2.5$ either an ultraluminous starburst or an obscured AGN could match the 24 μm data. We note that although the BC03 stellar population model, which best fits the ACS through IRAC photometry at $z \approx 2.5$, is heavily reddened, it is not actually forming stars at the time it is observed, but is instead a poststarburst object whose ultraviolet light is fading away. The 24 μm detection would instead imply active star formation with a luminosity $>10^{12}\ L_{\odot}$, which would have to be completely hidden by dust at shorter wavelengths.

5. SPECTROSCOPIC OBSERVATIONS

The main result from § 4 is that HUDF-JD2 is either an unusually massive galaxy at $z \approx 6.5$ or a dusty galaxy at $z \approx 2.5$. In both cases, the best-fitting models suggest a poststarburst (i.e., evolved) stellar population, in which case we might expect the galaxy to have very weak or no emission lines in its spectra. On the other hand, the detection at 24 μm would imply the presence of dust-obscured star formation or an active nucleus. In order to attempt to measure a redshift for HUDF-JD2 and to further constrain its nature, we have searched for spectral features (or their absence) in optical and near-infrared spectra taken with a variety of telescopes and instruments. We describe these observations here.

HUDF-JD2 was observed for 4.8 hr with FORS2 on the VLT UT1 in service observing on several occasions from UT 2005 February 18 through March 4, using a 1″ slit width and the 600z holographic grism. The observations covered the wavelength range 0.749–1.075 μm, corresponding to $5.15 < z(\mathrm{Ly}\alpha) < 7.84$, with spectral resolution $R = \lambda/\Delta\lambda \approx 1400$. No significant emission features or continuum were detected. Based on the measured background noise and simulations adding artificial emission lines to the data, we estimate that detection flux limits for an unresolved emission line falling in between the strong OH lines are $(2\text{–}4) \times 10^{-18}$ ergs s^{-1} cm^{-2} in the range $\lambda\lambda$0.912–0.973 μm, corresponding to $z(\mathrm{Ly}\alpha) = 6.5$–7.0.

At wavelengths corresponding to Lyα at $z > 6$, the detection of prominent emission lines may be hindered by the forest of strong OH night-sky lines. Therefore, we have also analyzed the *HST* ACS G800L grism images available from the GRAPES project (Pirzkal et al. 2004), which provides continuous wavelength coverage with a smooth sky background at a low spectral resolution of $\sim$80 Å. The observations were carried out at four different position angles to facilitate disentangling overlapping spectra in the slitless data, with a total exposure time of 25.6 hr. A spectrum was extracted over a spatial width of 0.″25 at the nominal position of HUDF-JD2, covering the wavelength range 0.55–1.05 μm. Again, no features were seen at >3 σ level, with a 3 σ limiting emission-line flux limit of 3×10^{-18} ergs cm^{-2} s^{-1} over the range 9000–9600 Å.

At near-infrared wavelengths, HUDF-JD2 was observed for 2 hr with NIRSPEC on Keck II on UT 2005 January 17 in clear skies and 0.″8–1″ FWHM seeing. The observations used the low-resolution mode with the 75 line mm^{-1} grating and a slit width of 0.″76, for a net spectral resolution $R \approx 1500$. The observations covered the wavelength range 0.947–1.12 μm [$6.79 < z(\mathrm{Ly}\alpha) < 8.21$], complementing that examined with FORS2. Again, no spectral features were detected. Over most of the range, the mean 3 σ limiting flux for an emission line with rest-frame velocity FWHM = 300 km s^{-1} from a point source is 5.0×10^{-18} ergs s^{-1} cm^{-2} (varying from 5×10^{-18} to 1×10^{-17} ergs s^{-1} cm^{-2} depending on the proximity to OH sky lines).

Finally, the object was also observed at yet longer wavelengths with the Gemini South telescope. In a 4.8 hr exposure with the Gemini Near-Infrared Spectograph (GNIRS) we used the short blue camera in cross-dispersed mode, which simultaneously covers the *zJHK* bands with continuous coverage from 0.94 to 2.53 μm. The 32 line mm^{-1} grating and a slit width of 0.″45 give a net spectral resolution $R \approx 1100$. Again, no convincing emission lines were detected. The observed GNIRS 3 σ median limits in *zJHK* bands, representing a sensitivity limit of 50% of the spectrum in each order, are 1.8×10^{-18}, 1.4×10^{-18}, 3.5×10^{-18}, and 3.1×10^{-18} ergs s^{-1} cm^{-2}, respectively.

Collectively, these data provide various upper limits to the ongoing star formation rate and the contribution from AGNs, as discussed in § 4.3. For the favored high-redshift hypothesis, assuming a Salpeter IMF, the FORS2, NIRSPEC, and GNIRS data set limits for the detection of unabsorbed Lyα emission corresponding to star formation rates of 1–5 $M_{\odot}$ yr^{-1} in the redshift range $5.2 < z < 8.2$, consistent with the quiescent state of the stellar population implied by the red UV continuum. Also, there are a number of emission-line features originating from AGNs, which lie in the FORS2 and GNIRS wavelength range covered by our spectroscopic observations (e.g., C IV, He II, and C III]). Although weak, nondetection of these lines is consistent with a highly obscured AGN in HUDF-JD2 at $z \sim 6.5$.

The longer wavelength coverage of the Gemini GNIRS data allows us to test the alternative hypothesis that HUDF-JD2 is a dusty galaxy whose 24 μm emission is produced by an ultraluminous infrared starburst or AGN. At $1.9 < z < 2.8$, Hα is shifted into the wavelength range covered by the GNIRS *K*-band observations. At $z = 2.3$, the 3 σ GNIRS line flux detection limit corresponds to a luminosity limit for redshifted Hα of 9×10^{40} ergs s^{-1}. This luminosity is quite typical for Hα emission from local ULIRGs: >55% of the ULIRGs in the sample of Armus et al. (1989) have Hα luminosities larger than this value. The [O III] 5007 Å line lies within the GNIRS *H*- and *K*-band spectral range for $1.9 < z < 4.0$, with a gap around $z \approx 2.8$ due to atmospheric absorption. This line can be as strong as the Hα line in dusty, red galaxies at these large redshifts (van Dokkum et al. 2005) and may be expected to be particularly strong if the 24 μm emission is due to the presence of an obscured AGN. In practice, the spectroscopic limits on emission-line detection vary substantially with wavelength (and hence, with redshift) due to the strong atmospheric OH emission lines and water absorption bands. The nondetection

of emission lines in the infrared spectra therefore sets a useful, if not definitive, limit on the possibility that HUDF-JD2 is a dusty starburst galaxy or AGN at lower redshift. Moreover, signatures of Lyα and C IV are seen in dusty submillimeter observations and AGNs at $z \sim 2.5$ (Chapman et al. 2003). If HUDF-JD2 resembles these dusty galaxies at their respective redshifts, we would then expect to detect these lines in its spectra.

6. DISCUSSION

As described in § 4, the photometry of HUDF-JD2 is best fit by a two-component model consisting of a passive stellar population with an age of several hundred million years and little dust reddening, observed at $6 < z < 7.5$ (95% confidence interval), and an AGN producing the light at longer (24 μm) wavelengths. The redshift is large but not unprecedented: other galaxies and quasars have been spectroscopically confirmed at similarly large redshifts, although we note that the photometric redshift probability distribution (Figs. 4 and 5) extends up to $z \approx 8.5$.

The most striking aspect of HUDF-JD2 in this hypothesis, however, is the large implied stellar mass and the significant age implied by the photometric data, particularly from *Spitzer* IRAC. Unlike Lyα emitters or UV-bright LBGs that have been discovered at $z > 6$, HUDF-JD2 appears *not* to be forming stars rapidly, but rather to be fading after an earlier starburst episode that took place at much higher redshift, $z_{\rm form} > 10$. The implied stellar mass for a Salpeter IMF, approximately $6 \times 10^{11}\ M_{\odot}$, is 4 times more massive than that of an L_* galaxy in the local universe ($M_* = 1.4 \times 10^{11}\ M_{\odot}$ for a Salpeter IMF and our adopted cosmology; Cole et al. 2001). It is about 50 times greater than that of a typical (L_*) LBG at $z \approx 3$ ($M_* \sim 10^{10}\ M_{\odot}$; Papovich et al. 2001) and is even large compared to the masses that have been estimated for redder, more evolved galaxies from infrared-selected samples at $z \approx 2$–3 ($M_* \sim 10^{11}\ M_{\odot}$; Franx et al. 2003; Daddi et al. 2004; Yan et al. 2004; Labbé et al. 2005). The implied stellar mass may be reduced somewhat if an obscured active nucleus, which is presumed to produce the 24 μm emission, contributes significantly to the flux in the IRAC bands. The model considered in § 4.3, using a redshifted analog to Mrk 231, would reduce the derived stellar mass by about a factor of 2, whereas the redshifted NGC 1068 model would have virtually no impact on the derived host galaxy properties.

The estimated high mass is also interesting in other respects. Although clearly resolved (§ 3), one might expect HUDF-JD2 to have a larger angular diameter due to a mass-radius relation (Trujillo et al. 2004), extrapolated to $z \sim 6.5$. In fact, we find this to lie on a reasonable extrapolation of the radius-redshift relation (Ferguson et al. 2004), derived from a much less massive sample of Lyman break galaxies.

Indeed, evidence for established stellar populations at $z \simeq 6$–7 is becoming stronger from deep *Spitzer* data. Recently, a strongly lensed galaxy was discovered with a likely redshift $z \sim 6.8$ (Kneib et al. 2004), with a clear detection by *Spitzer* at 3.6 and 4.5 μm (Egami et al. 2005). Its SED is consistent with a post-starburst galaxy with an age of ~50–200 Myr. Compared to that object, HUDF-JD2 has redder colors and a stronger Balmer break, indicating an older age (400–1000 Myr). It is also approximately 100 times more luminous in the rest-frame B band (observed 3.6 μm), after taking into account the lensing amplification estimated by Kneib et al. The redder SED of HUDF-JD2 also implies a larger stellar mass-to-light ratio (M/L), and thus a total stellar mass that is ~500–1400 times larger than that estimated by Egami et al.

A number of unlensed $z \approx 5$–6 i_{775}-dropout LBGs have also been detected in the GOODS IRAC data (Eyles et al. 2005; Yan et al. 2005). These objects are 5–30 times fainter than HUDF-JD2, with bluer optical-IR colors that imply active (or very recent) star formation and smaller stellar M/L. Their estimated stellar masses, again for a Salpeter IMF, range from 0.5 to $5 \times 10^{10}\ M_{\odot}$. The model fits to HUDF-JD2 suggest that it is at least an order of magnitude more massive and that its active star formation phase ended several hundred years prior to the redshift at which it is observed. Finally, we note that the six z_{850}-band dropout candidates reported by Bouwens et al. (2004) as galaxy candidates at $z = 7$–8 are all much fainter than HUDF-JD2, or are undetected, in the GOODS IRAC images.[15]

Given the remarkably large stellar mass that we infer for HUDF-JD2 at $z \approx 6.5$ and the absence of definitive spectroscopic confirmation for that redshift, it is prudent to consider alternative hypotheses. These might include an AGN contribution to the light, gravitational lensing, changes to the stellar population models (e.g., to the IMF), or the possibility that the object is at $z < 6$, possibly an extremely red object or even an unusual very red star.

We already explored the effect of an AGN on the estimated mass of HUDF-JD2 (§ 4.3) and concluded that this could reduce its mass by ~2. Concerning the hypothesis of gravitational lensing, HUDF-JD2 is located 7.″3 away from a foreground spiral galaxy at $z = 0.457$. At this large impact parameter from an isolated (noncluster) galaxy, we would expect little or no amplification from gravitational lensing, nor do we see evidence for elongation or multiple imaging that might suggest strong lensing. It also seems unlikely that HUDF-JD2 could be a red star within our own galaxy. Dickinson et al. (2000) considered stellar explanations for another J-band dropout object from the Hubble Deep Field North in some detail and found that only heavily dust-enshrouded objects such as some carbon stars or Mira variables could match the very red infrared colors. Such objects would be far brighter than HUDF-JD2 unless they were located far outside our own Galaxy, at distances of many Mpc. Moreover, HUDF-JD2 is clearly extended in the NICMOS H_{160} images, making a stellar origin unlikely.

From the stellar population model fitting discussed in § 4 (see Figs. 3–5), the most likely alternative to the passive, $z \approx 6.5$ scenario is that HUDF-JD2 is a heavily dust-obscured, poststarburst galaxy at lower redshift. Such models generally do not match the observed SED well because of the break between the near-infrared and IRAC wavelengths, resulting in poorer χ^2 overall. In addition, these models require both an absence of recent star formation *and* heavy dusty extinction in order to be consistent with the extraordinarily deep optical detection limits provided by the ACS HUDF data. As discussed in § 5, the nondetection of line emission in the Gemini GNIRS data can be used to argue against a dusty starburst at lower redshift, although at certain redshifts, line emission might be obscured by atmospheric features or fall outside the spectral range of the existing data.

The stellar mass inferred from SED modeling could be reduced by adopting an IMF that is deficient (relative to Salpeter) in lower mass stars, such as that proposed by Chabrier (2003). However, this would not substantially change the mass *relative* to that of other galaxies at similar or lower redshifts, unless we appeal to an IMF that varies substantially from galaxy to galaxy or as a function of redshift.

Recently, Maraston (2005) has presented models that include a greater contribution to the red optical and near-infrared light

[15] Two of the Bouwens et al. (2004) objects are close enough to brighter foreground galaxies to make the IRAC measurements difficult without sophisticated deblending, but they would have been easily visible if they were as bright as HUDF-JD2. At least two of the Bouwens et al. objects, UDF 033238.79−274707.1 and UDF 033242.56−274656.6, appear to be individually detected in the GOODS IRAC 3.6 μm image, but at very faint fluxes.

from thermally pulsating AGB stars at stellar population ages of a few hundred Myr compared to traditional models such as BC03 or Starburst99. The Maraston models have redder UV to near-IR colors and smaller M/L at the wavelengths spanned by IRAC photometry at $z \approx 6.5$. For a simple stellar population with age 1 Gyr (i.e., equivalent to our best-fitting BC03 or Starburst99 models), the Maraston models have approximately 30% smaller M/L at rest-frame 1 μm (i.e., roughly the wavelength sampled by IRAC channel 4 at $z \approx 6.5$). We verified that the observed SED can be reproduced with somewhat younger ages, reduced formation redshift, and stellar mass. It is unlikely, however, that the mass could be reduced by more than a factor of 2.

If the $z > 6$ interpretation of HUDF-JD2 is correct, then this galaxy formed the bulk of its stars at very high redshift, $z > 9$, within a period of a few hundred Myr before entering a quiescent phase. Remarkably, this galaxy would have formed a stellar mass several times greater than that of our Milky Way (even allowing for IMF variations) and would have done so very rapidly, when the universe was only a few hundred million years old. Assuming the formation starburst lasted <100 Myr, as implied by the stellar population models, the star formation rate must have been $>5000\ M_\odot\ \mathrm{yr}^{-1}$, implying a remarkably luminous birth event, particularly at observed-frame mid-infrared wavelengths if the star formation was relatively unobscured. Such a massive galaxy is expected to host a supermassive black hole (SMBH) at its center, producing the observed 24 μm emission as discussed in § 4.3. Therefore, at $z > 6$, while HUDF-JD2 is forming a significant number of stars, the SMBH is expected to accrete a lot of mass.

It is instructive to estimate the mass of dark matter halo required to host the stellar mass of HUDF-JD2. Klypin et al. (2002) estimate the total (virial) and baryonic ($M_{\mathrm{stlr}} + M_{\mathrm{gas}}$) mass of the Milky way as $10^{12}\ M_\odot$ and $6 \times 10^{10}\ M_\odot$, respectively. Assuming the same ratio ($M_{\mathrm{bary}}/M_{\mathrm{tot}} = 0.06$) for HUDF-JD2 and 100% efficiency in converting baryons to stars, we estimate a dark matter halo mass of $10^{13}\ M_\odot$, required to host $6 \times 10^{11}\ M_\odot$ mass of HUDF-JD2. However, considering the universal $M_{\mathrm{bary}}/M_{\mathrm{tot}}$ ratio of 0.15, the dark matter halo mass reduces to $4 \times 10^{12}\ M_\odot$. Assuming the Sheth-Tormen modified Press-Schechter formalism (Sheth & Tormen 2002) and a ΛCDM model, we then predict a space density of $\sim 10^{-6}\ \mathrm{Mpc}^{-3}$ for such dark matter halos (Somerville 2005; Mo & White 2002), which is significantly smaller than that observed here (based on HUDF-JD2 alone). Should such a population exist, they are expected to be strongly clustered.

Analyzing optical through IRAC photometry for red, infrared-selected galaxies at $z \approx 2$–3, Labbé et al. (2005) and Yan et al. (2004) have argued that some are dominated by at least $10^{11}\ M_\odot$ of old stars that must have formed at $z \gg 5$. Similar arguments have been found in the literature concerning "red, dead" galaxies at almost any redshift, including extremely red objects at $z \approx 1$–2 (see McCarthy 2004 for a review) and giant elliptical galaxies in the local universe (Eggen et al. 1962). We estimate the expected colors of HUDF-JD2 when passively evolving the $z = 6.5$ SED-fit solution to $z \sim 2.5$, the average redshift of the distant, red galaxies (DRGs; Franx et al. 2003; Toft et al. 2005) and the upper redshift limit of the BzK-selected objects (Daddi et al. 2004). We predict $J - K = 2.9$, $i - K = 5.6$, $K - m(3.6\ \mu\mathrm{m}) = 0.7$, and $K_s \sim 20$ for HUDF-JD2 when evolved to $z = 2.5$. This agrees closely with the observed colors of the DRGs, estimated as $\langle J - K_s \rangle > 2.3$, $\langle i - K_s \rangle = 5$, and $\langle K_s - m(4.5\ \mu\mathrm{m}) \rangle = 0.9$ (Labbé et al. 2005). Moreover, given the predicted K_s-band magnitude, such evolved objects will be detected in the K20 (Mignoli et al. 2005) or *BzK* (Daddi et al. 2004) surveys. HUDF-JD2 might be seen as a progenitor to such galaxies and a sign that at least a few objects may have formed quite large masses of stars "monolithically" at very early times and evolved quiescently down to lower redshifts. Even if the source did not collapse monolithically, but arose from several subgalactic components that subsequently coalesced, it seems such early phases should be visible with future large-aperture telescopes such as the Thirty Meter Telescope and the *James Webb Space Telescope*. The mere existence of objects with such large star formation rates at very high redshift would have important implications for the reionization of the intergalactic medium, and we discuss this further in a companion paper (Panagia et al. 2005).

This paper is based on observations taken with the NASA/ESA *Hubble Space Telescope*, which is operated by AURA, Inc., under NASA contract NAS5-26555, the *Spitzer Space Observatory*, and the W. M. Keck Observatories. Support for this work, part of the *Spitzer Space Telescope* Legacy Science Program, was provided by NASA through contract 1224666 issued by the Jet Propulsion Laboratory, California Institute of Technology, under NASA contract 1407. We acknowledge award of Director's Discretionary Time at the Gemini South observatory and the Very Large Telescope (VLT) at Cerro Paranal, Chile. We are grateful to Matt Mountain and Phil Puxley for making the spectroscopic observations possible. We acknowledge an anonymous referee for carefully reading the manuscript and for very constructive comments. We are grateful to Dave Alexander for his help in measuring the *Chandra* detection limit and to the GRAPES team for the use of their data.

REFERENCES

Ajiki, M., et al. 2004, PASJ, 56, 597
Alexander, D. M., et al. 2003, AJ, 126, 539
Armus, L., Heckman, T. M., & Miley, G. K. 1989, ApJ, 347, 727
Bertin, E., & Arnout, S. 1996, A&AS, 117, 393
Bouwens, R. J., et al. 2004, ApJ, 606, L25
Braito, V., et al. 2004, A&A, 420, 79
Bruzual A., G., & Charlot, S. 2003, MNRAS, 344, 1000 (BC03)
Bunker, A., J. Stanway, E. R., Ellis, R. S., & McMahon, R. 2004, MNRAS, 355, 374
Calzetti, D., Armus, L., Bohlin, R. C., Kinney, A. L., Koornneef, J., & Storchi-Bergmann, T. 2000, ApJ, 533, 682
Chabrier, G. 2003, PASP, 115, 763
Chapman, S. C., Blain, A. W., Ivison, R. J., & Smail, I. R. 2003, Nature, 422, 695
Chary, R., & Elbaz, D. 2001, ApJ, 556, 562 (CE01)
Chen, H.-W., & Marzke, R. 2004, ApJ, 615, 603
Cole, S., et al. 2001, MNRAS, 326, 255
Daddi, E., Cimatti, A., Renzini, A., Fontana, A., Mignoli, M., Pozzetti, L., Tozzi, P., & Zarmorani, G. 2004, ApJ, 617, 746
Dickinson, M., & Giavalisco, M. 2003, in The Mass of Galaxies at Low and High Redshift, ed. R. Bender & A. Renzini (Berlin: Springer), 324
Dickinson, M., et al. 2000, ApJ, 531, 624
Donley, J. L., Rieke, G. H., Rigby, J. R., & Perez-Gonzales, P. G. 2005, ApJ, 634, in press (0507676)
Egami, E., et al. 2005, ApJ, 618, L5
Eggen, O. J., Linden-Bell, D., & Sandage, A. R. 1962, ApJ, 136, 748
Eyles, L., Bunker, A., Stanway, E., Lacy, M., Ellis, R. S., & Doherty, M. 2005, MNRAS, in press (astro-ph/0502385)
Ferguson, H. C., et al. 2004, ApJ, 600, L107
Franx, M., et al. 2003, ApJ, 587, L79
Galliano, E., Alloin, D., Granato, G. L., & Villar-Martin, M. 2003, A&A, 412, 615
Giacconi, R., et al. 2002, ApJS, 139, 369
Giavalisco, M. 2002, ARA&A, 40, 579
Giavalisco, M., et al. 2004a, ApJ, 600, L103
———. 2004b, ApJ, 600, L93
Klypin, A., Zhao, H. S., & Somerville, R. S. 2002, ApJ, 573, 597
Kneib, J., Ellis, R. S., Santos, M. R., & Richard, J. 2004, ApJ, 607, 697
Labbé, I., et al. 2005, ApJ, 624, L81

Leitherer, C., et al. 1999, ApJS, 123, 3
Loeb, A., & Barkana, R. 2001, ARA&A, 39, L19
Madau, P. 1995, ApJ, 441, 18
Maraston, C. 2005, MNRAS, 362, 799
Matt, G., Fabian, A. C., Guainazzi, M., Iwasawa, K., Bassani, L., & Malaguti, G. 2000, MNRAS, 318, 173
McCarthy, P. M. J. 2004, ARA&A, 42, 477
Mignoli, M., et al. 2005, A&A, 437, 883
Mo, H. J., & White, S. D. M. 2002, MNRAS, 336, 112
Ouchi, M., et al. 2004, ApJ, 611, 660
Panagia, N., Fall, S. M., Mobasher, B., Dickinson, M., Ferguson, H. C., Giavalisco, M., Stern, D., & Wiklind, T. ApJ, 2005, 633, L1
Papovich, C., Dickinson, M., & Ferguson, H. C. 2001, ApJ, 559, 620
Pirzkal, N., et al. 2004, ApJS, 154, 501
Reddy, N. A., & Steidel, C. C. 2004, ApJ, 603, L13
Rhoads, J. E., et al. 2004, ApJ, 611, 59
Sheth, R. K., & Tormen, G. 2002, MNRAS, 329, 61
Somerville, R. S. 2005, in Multiwavelength Mapping of Galaxy Formation and Evolution, ed. R. Bender & A. Renzini (Garching: ESO), in press (astro-ph/0401570)
Somerville, R. S., Primack, J. R., & Faber, S. M. 2001, MNRAS, 320, 504
Steidel, C. C., Adelberger, K. L., Shapley, A. E., Pettini, M., Dickinson, M., & Giavalisco, M. 2003, ApJ, 592, 728
Stiavelli, M., Fall, S. M., & Panagia, N. 2004, ApJ, 600, 508
Thompson, R., et al. 2005, AJ, 130, 1
Toft, S., van Dokkum, P., Franx, M., Thompson, R. I., Illingworth, G. D., Bouwens, R. J., & Kriek, M. 2005, ApJ, 624, L9
Trujillo, I., et al. 2004, ApJ, 604, 521
van Dokkum, P., Kriek, M., Rodgers, B., Franx, M., & Puxley, P. 2005, ApJ, 622, L13
Vázquez, G. A., & Leitherer, C. 2005, ApJ, 621, 695
Yan, H., & Windhorst, R. A. 2004, ApJ, 612, L93
Yan, H., et al. 2004, ApJ, 616, 63
———. 2005, ApJ, 634, 109